Advanced Functional Materials

ADVANCED FUNCTIONAL MATERIALS
www.afm-journal.de

RESEARCH ARTICLE OPEN ACCESS

Water Adsorption-Induced Color Sensor: Insight Into the Sensing Mechanism and Interfacial Engineering for Improved Responsiveness

Tai Kobayashi[1] | Ryosuke Nishikubo[1,2] | Yusuke Tomiyori[3,4] | Fumitaka Ishiwari[1,2,5] | Daisuke Asakura[6] | Eiji Hosono[6] | Miho Kitamura[7] | Hisao Kiuchi[3,8] | Yoshihisa Harada[3] | Akinori Saeki[1,2]

[1]Department of Applied Chemistry, Graduate School of Engineering, The University of Osaka, Suita, Osaka, Japan | [2]Innovative Catalysis Science Division, Institute for Open and Transdisciplinary Research Initiatives (ICS-OTRI), The University of Osaka, Suita, Osaka, Japan | [3]Institute for Solid State Physics (ISSP), The University of Tokyo, Kashiwa, Chiba, Japan | [4]AGC Inc., Yokohama, Kanagawa, Japan | [5]Faculty & Graduate School of Urban Environmental Science, Tokyo Metropolitan University, Tokyo, Japan | [6]Research Institute for Energy Efficient Technologies, National Institute of Advanced Industrial Science and Technology (AIST), Tsukuba, Ibaraki, Japan | [7]NanoTerasu Center, National Institutes for Quantum Science and Technology (QST), Sendai, Miyagi, Japan | [8]Research Center for Energy and Environmental Materials (GREEN), National Institute for Materials Science (NIMS), Tsukuba, Ibaraki, Japan

Correspondence: Ryosuke Nishikubo (nishikubo@chem.eng.osaka-u.ac.jp) | Hisao Kiuchi (kiuchi.hisao@nims.go.jp) | Yoshihisa Harada (harada@issp.u-tokyo.ac.jp) | Akinori Saeki (saeki@chem.eng.osaka-u.ac.jp)

Received: 21 January 2026 | **Revised:** 11 May 2026 | **Accepted:** 17 June 2026

Keywords: antimony | color-sensing | photodetector | photovoltaics | TiO_2

ABSTRACT

Color-sensitive photodetectors are at the forefront of next-generation light- and image-sensing research. In this context, a photovoltaic device employing SbSI:Sb_2S_3 and TiO_2 as the visible light absorber and electron transport material, respectively, exhibits a unique wavelength-dependent photovoltage effect and its reversible output in response to changing humidity levels. However, the specific functions of the individual layers of the device and their interaction with water remain largely unknown. In this study, we perform in situ X-ray absorption spectroscopy (XAS) of thin films under humidity-controlled conditions to reveal the interaction between water and the photovoltaic layers. The oxygen K-edge XAS data reveal the adsorption of water molecules onto TiO_2. Ultraviolet (UV) irradiation of TiO_2 can trigger photochemical reactions of the adsorbed water at the interface, which is considered to contribute to changes in the photovoltage. Based on this finding, we introduce hydrophilic layers between TiO_2 and SbSI:Sb_2S_3 to promote the accumulation of water in the devices, which successfully enhance both the wavelength sensitivity and response speed. Finally, we demonstrate color recognition with various irradiation intensities, thereby broadening the scope and applications of unique wavelength-responsive single-cell photovoltaics.

1 | Introduction

Photodetectors are essential components of information technology that enable diverse optical applications, such as light sensing, image capture, and optical communications [1–3]. A critical requirement for next-generation photodetectors is responsiveness across multiple wavelengths. Photodetectors and photovoltaic (PV) devices typically exhibit a linear increase in the short-circuit current density (J_{SC}) with incident light intensity (P_{in}), whereas the open-circuit voltage (V_{OC}) increases marginally with the logarithmic value of P_{in}, as described by Shockley's diode equation [4, 5]. Besides, the PV output is generally independent of the irradiation wavelength if the photon energy is greater than the bandgap energy of the photoactive layer. Thus, the wavelength of the irradiated light can be distinguished using color filters (e.g., red, green, blue (RGB)) or spatial separation through prisms.

In 2022, we reported the unprecedented filter-less wavelength dependence of the photovoltage in a single cell composed of an antimony sulfiodide and sulfide ($SbSI:Sb_2S_3$, named ASIS) photoactive layer [6, 7]. The device structure was fluorine-doped tin oxide (FTO)/TiO_2/ASIS/PCPDTBT/Au [PCPDTBT: poly(cyclopentadithiophene-benzothiadiazole)], which exhibited low and high photovoltages under ultraviolet (UV) and visible-light irradiation, respectively (Figure S1a,b). Interestingly, this wavelength-dependent photovoltaic effect (WDPE) is enhanced under high-humidity conditions. Although SbSI and Sb_2S_3 have received significant attention in the areas of PV [8–11] ferroelectric materials and sensors [12–14] and photocatalysts [15, 16], their WDPE behavior remains largely unexplored.

Recently, remarkable progress has been made in the development of multicolor-sensitive photodetectors. Two types of devices exist: dual-band photodetectors and color-selective photodetectors. The former is constructed from two different photoactive materials with different bandgaps that exhibit responses in two distinct wavelength regions (450–500 and 650–800 nm) [17–19]. However, they are unable to discern the irradiated wavelength without a filter. In contrast, color-selective photodetectors exhibit dynamic tunability of color detection [20–23]. For instance, Lan et al. invented an organic photodetector that selectively detects 400–500 or 520–620 nm light under positive and negative biases, respectively [21]. They also demonstrated a 2D image-capturing device. Min et al. reported the wavelength-specific photocurrent transient of a perovskite photodetector [24], which showed charge carrier dynamics partly similar to those of our WDPE. Notably, their single-junction self-powered photodetector successfully recognized a wide range of colors (350–750 nm) in the photocurrent waveform. Color-selective detection is advantageous for enhancing spatial resolution and reducing the size of imaging devices. However, color detection based on the output voltage using a single-junction cell has only been achieved within our WDPE framework. This characteristic allows for the simultaneous detection of light intensity and wavelength from the output current and voltage, respectively.

A significant challenge associated with the WDPE phenomenon is understanding its mechanism. Szaniawski et al. reported wavelength-dependent photovoltages in $Cu(In,Ga)Se_2$ PVs in which the breakdown voltage temporarily decreased upon UV irradiation [23]. These phenomena were attributed to the differences in the penetration depths of UV and visible light. However, we observed that WDPE remained unaffected by the direction of irradiation, whether from the bottom or top, suggesting that the light penetration depth was not the origin of the WDPE. Therefore, WDPE likely originates from more complex photochemical reactions involving charge carriers, water (or polar solvent) molecules, and the materials that compose the device. Through various evaluations, we elucidated three key properties: (i) WDPE behavior depends significantly on the selection of the electron transport material (ETM) and hole transport material (HTM). In particular, a device containing TiO_2 (ETM) exhibited particularly enhanced WDPE. (ii) Strong WDPE behavior occurs under high-humidity conditions. (iii) WDPE is likely related to the generation of trap sites induced by UV irradiation. Property (i) suggests that the interfaces between these materials and the active layer play a crucial role. Both transient photovoltage (TPV) [25] and charge extraction by linearly increasing the voltage (CELIV) [26, 27] exhibited accelerated recombination under UV irradiation. TPV measurement results indicate that the lifetime decreased from 31.5 to 14.9 ms upon UV irradiation, and a comparable decay in lifetime was also observed in CELIV measurement (Figure S1c,d). Electron spin resonance (ESR) measurements under visible-light irradiation [28, 29] exhibited reduced hole densities in the HTM upon additional UV irradiation (Figure S1e,f). This contrasts with the behavior of conventional PV devices, providing direct evidence of accelerated recombination and/or trapping rather than an increase in hole density upon UV irradiation.

Despite these findings, the layers that play specific roles in the WDPE remain unclear. Various measurements of PV devices, including current density–voltage (*J*–*V*) scanning, TPV, CELIV, and impedance spectroscopy, inherently comprise contributions from multiple layers, making it challenging to isolate the role of each layer. Although ESR clearly detected a signal attributed to holes in the organic HTM, no signals from other inorganic layers, such as TiO_2 and ASIS, were observed. To assess the presence of low-density water molecules at the interface and study photochemical reactions under light exposure, we must utilize an advanced spectroscopic technique with intense X-rays from a synchrotron facility.

In this study, we performed in situ X-ray absorption spectroscopy (XAS) to determine the location of trapped water molecules in the FTO/TiO_2/ASIS/PCPDTBT/Au device. A specially designed ambient-pressure cell was used to enable humidity-controlled measurements of the film samples. The intensity of the oxygen (O) K-edge XAS spectra increased under high-humidity conditions. This suggests that water molecules can easily penetrate the device structures and adsorb onto TiO_2 surfaces. The water molecules adsorbed on the TiO_2 layer were correlated with a dramatic change in V_{OC} under UV irradiation. Subsequently, photocatalytic reactions are induced on TiO_2, which may produce ionic species such as H^+ and OH^-, working as temporal trap sites. Based on these results, hydrophilic polymers were introduced into the device to improve the sensitivity and response speed of the wavelength-dependent photovoltage. Polystyrene sulfonic acid significantly improved the response speed. Among representative self-powered color-sensitive photodetectors, our device exhibited the fastest response to photovoltage-based wavelength recognition (Table S1). These findings are expected to pave the way for improving the multicolor sensing ability of WDPE devices.

2 | Results and Discussion

2.1 | Mechanism of WDPE

2.1.1 | Analysis of Water Penetration Behavior via In Situ XAS

Four thin-film samples with different stacking structures on glass substrates were prepared for O K-edge XAS measurements: single layers of TiO_2, ASIS, and PCPDTBT, and a triple layer of TiO_2/ASIS/PCPDTBT. The measurement setup of the in situ XAS is shown in Figure S2. Water adsorption was evaluated based on the change in the X-ray absorption intensity at the O K-edge (520–550 eV). The obtained O K-edge XAS spectra of the glass

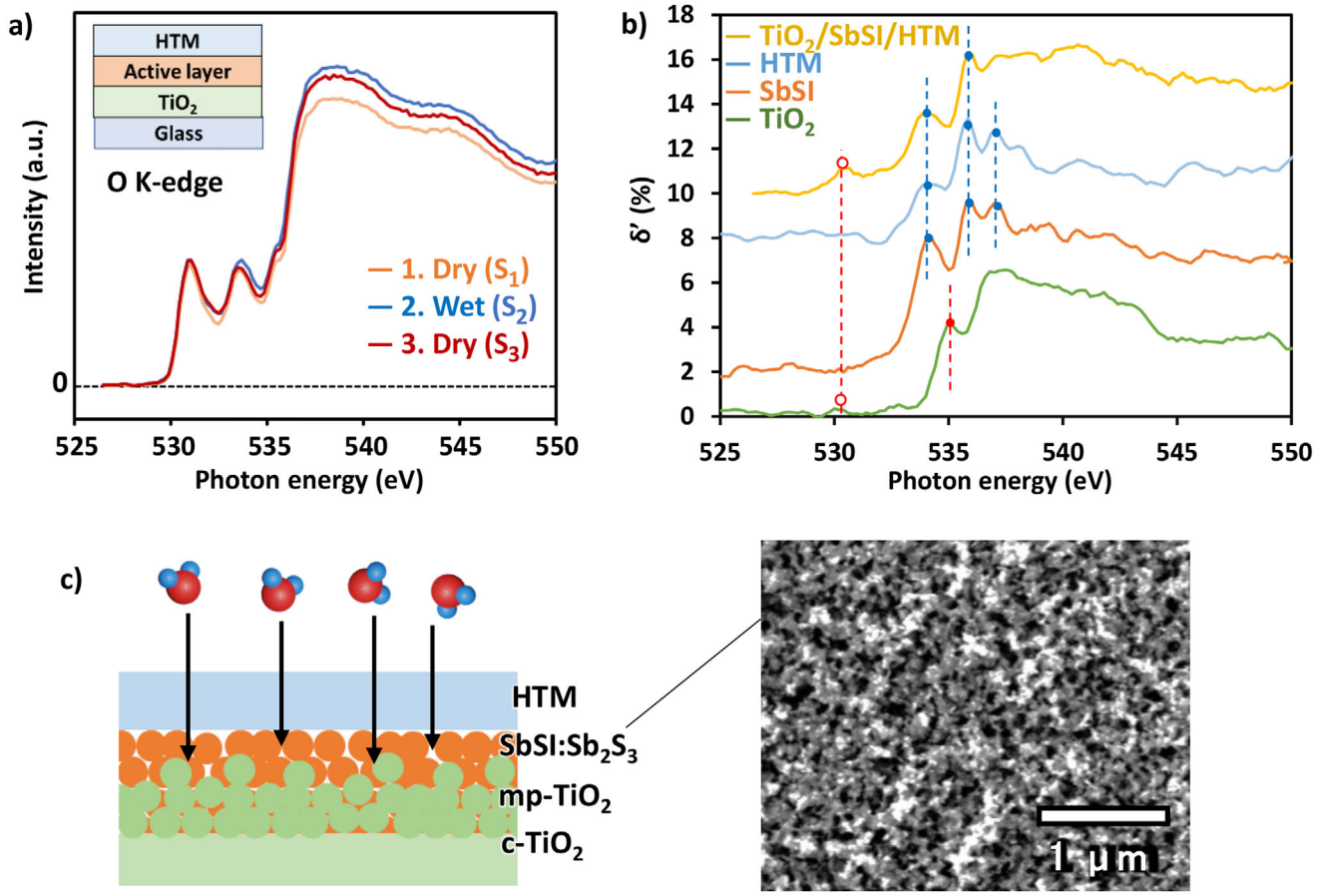

FIGURE 1 | (a) O K-edge XAS spectra of a triple layer measured under controlled humidity. (b) Corrected difference XAS spectra ratios (δ') of single layers and a triple layer. The correction procedure is shown in Figure S5. The peaks attributed to H_2O gas and liquid-like H_2O are marked with blue and red dots, respectively. The pre-edge peak attributed to H_2O–TiO_2 interaction is marked with red circles. The spectra of SbSI, HTM, and a tri-layer are shifted along the vertical axis for easier comparison. (c) Schematic of water molecule penetration and adsorption onto the layered samples. The SEM image of ASIS on TiO_2 is appended, which is taken from our previous report [6].

substrate, TiO_2, ASIS, HTM single layers, and TiO_2/ASIS/HTM triple layer are shown in Figure S3 and Figure 1a. The broad, intense absorption at 535–550 eV in these samples was attributed to the oxygen in the TiO_2 and glass (SiO_2) substrates [30, 31] along with trivial contributions from water. Sharp peaks appeared at 531.0 and 533.5 eV in the TiO_2 single layer and TiO_2/ASIS/HTM triple layer (Figure S3c; Figure 1a), which are attributed to the oxygen in TiO_2 [32]. The measurement for each sample was performed in the order of first: dry (S_1), second: wet (S_2), and third: dry (S_3) (where S denotes the XAS spectrum). A slight but distinct increase and then decrease in intensity was observed in the 535–550 eV region in response to the humidity value (wet: 70% RH and dry: 0% RH). This change is attributed to the adsorption and desorption of water. To compensate for the large background coming from the glass substrate and layer components, we calculated the difference spectra ratios (δ). Owing to the X-ray-induced hydrophilization (Figure S4) [33], S_1 and S_3 were not the same. Consequently, the hydrophilization effect was compensated for as much as possible by linear interpolation, as shown in Figure S5.

Figure 1b shows the corrected difference spectra ratios (δ') of single- and triple-layer samples. The difference spectra ratios without correction are shown in Figure S6 as a reference. The peaks of H_2O gas and liquid-like H_2O are marked by blue and red dots, respectively, and the broad difference spectrum with small sharp peaks at 534, 536, and 537 eV is attributed to a mixture of liquid and gaseous water [32, 34]. Water gas is derived from humidified gas flowing through the space between the SiC membrane and film (a few microns). Our observations are consistent with those of Nordlund et al., who reported that water adsorbed onto a metal catalyst exhibits O K-edge XAS spectra similar to those of ice and liquid water [35]. Notably, the TiO_2 and TiO_2/ASIS/HTM films exhibited a pre-edge at 530.5 eV marked by red circles. A similar extra peak was also observed in H_2O-adsorbed TiO_2, as described in a previous report [36], suggesting the adsorption of H_2O onto TiO_2 [37, 38]. The triple-layer film also exhibited an enhanced broad signal at 538–543 eV, which is specific to solid H_2O. Assuming a simple SiO_2/TiO_2/H_2O triple-layer model and calculating the integral intensity ratio at 550 eV in the glass/TiO_2 spectra (Note S1 and Tables S2 and S3), the thickness of the adsorbed water was estimated to be 10.0–12.4 nm. Because the ASIS layer is considerably thin (around 40 nm) and has a mesoporous morphology (Figure 1c), water molecules seem to penetrate it easily. A possible concern when comparing the bare TiO_2 and the fully layered sample is the signal attenuation caused by the overlayers. However, the HTM (PCPDTBT) and ASIS layers do not contribute to the O Kα fluorescence intensity but

function purely as attenuation filters because they do not contain oxygen. Comparing a 3-layer (glass/TiO_2/H_2O) and a 5-layer (glass/TiO_2/H_2O/ASIS/HTM) model (Tables S2 and S3) reveals that although the absolute spectral intensity and the intensity difference decrease by 18–38% considering the error margin, δ remain unchanged. However, δ' of the TiO_2 and TiO_2/ASIS/HTM films exhibit distinct profiles. This difference suggests that the ASIS layer may affect the wettability of TiO_2, which plays an important role in the WDPE response time, as discussed below.

Given that WDPE is most pronounced in TiO_2/ASIS/HTM devices and depends significantly on humidity, the interaction between TiO_2 and water is considered essential to the WDPE mechanism. To further probe the interfacial reactions, we also performed the Ti L_3-edge XAS on the TiO_2/ASIS/HTM tri-layer film under controlled humidity (Figure S7a). Characteristic changes were observed in the Ti L_3-edge XAS spectra after humidification, such a spectral change in the pre-edge region, together with a ≈0.1 eV shift of the peak at 457.9 eV toward lower photon energy. Notably, these changes are consistent with a previous report where TiO_2 nanoparticles in aqueous dispersion and under dry conditions were compared [39]. This result also supports the possibility of H_2O penetration into the stacked structure and its interaction with TiO_2. Sb M-edge XAS was also performed; although the fluorescence line of the Sb M-edge is approximately 100 eV lower than that of the O K-edge, the limited energy resolution (≈100 eV) of the SDD detector causes the weak Sb M-edge emission to be obscured by the overlapping tail of the intense O K-edge emission (Figure S7b).

2.1.2 | Role of the TiO_2 Layer on WDPE

To validate the importance of TiO_2 in WDPE, we studied the spectral responses of our devices. Figure 2a shows the wavelength-dependent J_{SC} and V_{OC} at 50% RH. The device structure and corresponding external quantum efficiency (EQE) spectra are shown in Figure S8. Importantly, the change in V_{OC} (ΔV) between the initial (0 s) and delayed (20 s) values was observed in the short wavelength region (<400 nm) (Figure 2b). This region corresponds to the bandgap energy of TiO_2 (Figure S9a), suggesting that TiO_2 is mainly responsible for the decrease in photovoltage. Under UV irradiation, the adsorbed H_2O may split into H^+ or OH^-, which are considered to be trapped at the ASIS/HTM and/or TiO_2/ASIS interface and serve as metastable electron/hole trap sites (Figure 2c). These ionic species are considered to gradually recombine and disappear, resulting in reversible device characteristics. We previously reported that the photovoltage response changed sublinearly with the irradiation wavelength (340–530 nm) [6]. Light with energy lower than the TiO_2 bandgap also induces a photovoltage drop to some extent. Considering the large Urbach energy of the TiO_2 film (650–680 meV) (Figure S9b), photoabsorption by the midgap states of TiO_2 can also induce a decrease in photovoltage.

To examine the necessity of the HTM and photoactive layer (ASIS), configurations of devices with control, devices without HTM, and devices without ASIS were also evaluated at 50% RH. Figure 3a shows the *J*–*V* curves of the HTM-less and ASIS-less devices. Despite the much lower power conversion efficiency than that of the control device, the HTM-less and ASIS-less devices exhibited diode behaviors. Importantly, the HTM- and ASIS-less devices also exhibited WDPE in time-dependent photovoltage (TDPV) (Figure 3b,c). In addition, we previously reported that WDPE was not observed in devices in which TiO_2 was replaced with SnO_2 or CdS as ETMs [6]. These results support the importance of the TiO_2 layer in WDPE. Notably, devices with different active layers, such as Pb perovskite and $Ag_xBi_yI_{x+3y}$, have never exhibited WDPE [6]. This is probably due to the dense film formation and/or the specific interfacial interaction with TiO_2, which hinder the interfacial photocatalytic reaction. In contrast, ASIS layer is advantageous for WDPE property because of its porous characteristics and the efficient carrier transport property. The porous morphology facilitates H_2O penetration. In addition, ASIS has efficient carrier transport property with the high EQE value (≈60%) [40], which facilitates observing the effect of increased trap-site.

We previously reported the influence of UV irradiation on carrier dynamics using transient photovoltage (TPV) and charge-extraction by linearly increasing voltage (CELIV) [6], and demonstrated that it results in the accelerated TPV transient (Figure S1c). However, the change in trap density has not been quantified. Herein, space-charge limited current (SCLC) measurement was performed with and without UV irradiation (Figure S10). Before and after a temporal UV irradiation (30 s), SCLC was immediately measured. The result exhibited an increase in trap density from 1.32×10^{17} to 1.53×10^{17} cm^{-3}, suggesting the generation of defect state upon UV irradiation.

2.2 | Improvement of Color-Sensing Characteristics

Inspired by the results showing that water can penetrate a device and adhere to the ASIS and/or TiO_2 layers, we introduced a thin hydrophilic polymer layer at the TiO_2/ASIS or ASIS/HTM interface to promote water penetration and adsorption and enhance the photochemical reaction of TiO_2. PSS (polystyrene sulfonic acid) and poly(vinyl alcohol) (PVA) were used as the hydrophilic polymers. Notably, the introduction of the polymers resulted in a dramatic improvement in the wavelength-photovoltage response (Figure 4a–e). The corresponding photocurrent decays are displayed in Figure S11. The reduced photocurrent is attributed to the introduction of an insulating layer such as PVA and PSS. The response time was calculated using a double exponential fitting of the TDPV curve obtained under UV irradiation. In particular, the introduction of the PSS layer dramatically improved the response speed to 150–390 ms (Figure 4f) compared to a few seconds (2–4 s) of the control (no interlayer) device. This rapid response is beneficial in sensing applications.

We further investigated the time-dependent photovoltage response under periodic UV pulse irradiation and continuous visible light irradiation. In the control device (Figure 4g), the additional rectangular UV irradiation (0.5 s) initially induced a rapid increase in the photovoltage owing to the increase in total photon density. This effect was clearly observed in the periodic response without irradiation of the 515 nm continuous light (Figure S12). Subsequently, a rapid decrease in photovoltage (= WDPE) of $\Delta V = 35 \pm 2.2$ mV was observed. The recovery

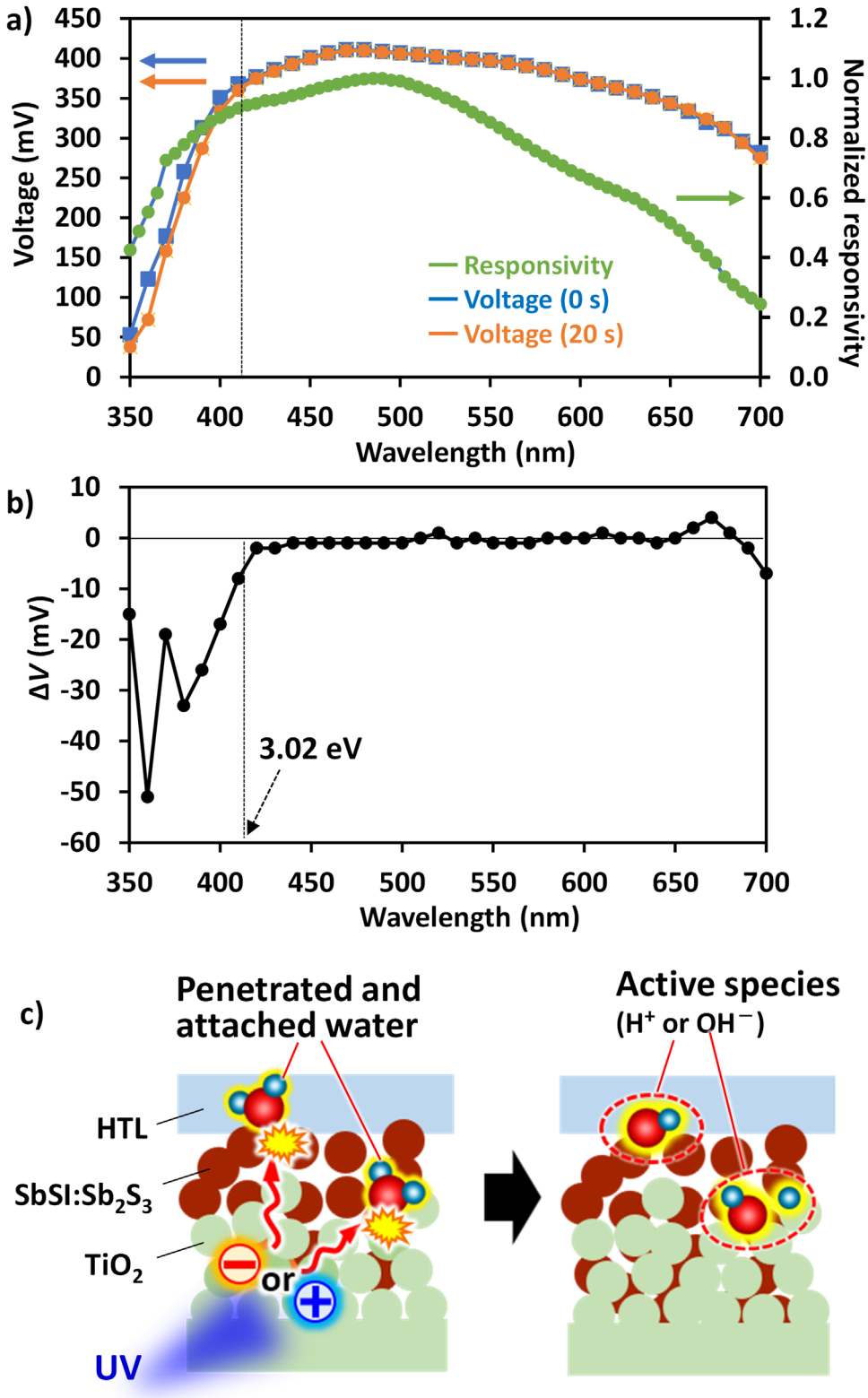

FIGURE 2 | (a) Spectrum-dependent photovoltage and responsivity. The retention time for each wavelength was set to 20 s. The blue and orange lines represent the photovoltage at the beginning and end of each step. (b) Spectrum-dependence of the change in photovoltage (ΔV) during the retention time. The bandgap energy of TiO_2 calculated from its photoabsorption spectrum is 3.02 eV (Figure S9). (c) The suggested mechanism of WDPE based on the data shown in Figures 1 and 2a,b.

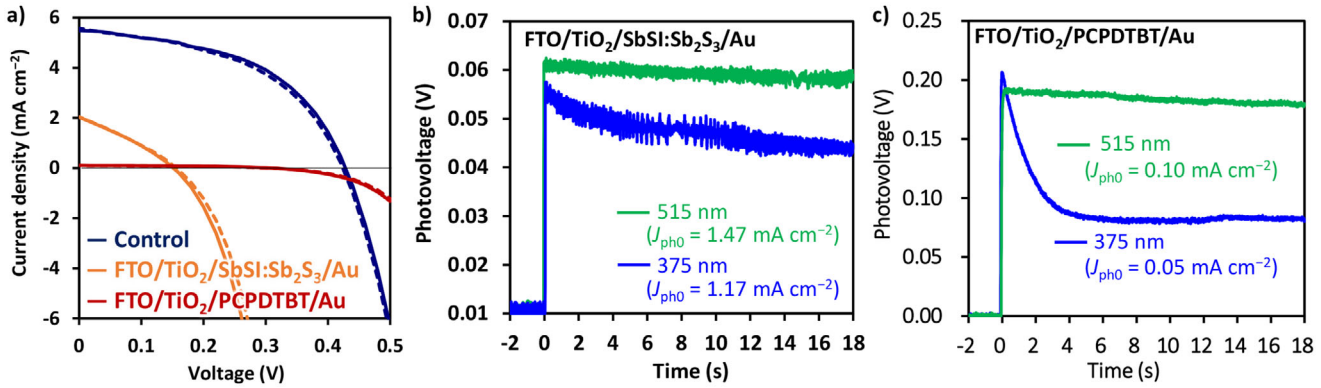

FIGURE 3 | (a) *J–V* curves of control, HTM-less, and ASIS-less devices measured under a 100 mW cm^{-2} Xe lamp. The solid and dotted lines indicate the forward and reverse scans, respectively. TDPV decays of (b) HTM-less device and (c) ASIS-less device. The corresponding photocurrent density (J_{ph0}) is displayed. The photon densities of the irradiated 315 nm (blue line) and 515 nm (green line) continuous lights are tuned to yield comparative current densities (6.1×10^{16} and 7.1×10^{16} photons cm^{-2} s^{-1} for the 315 and 515 nm lights in b), 3.3×10^{16} and 6.7×10^{17} photons cm^{-2} s^{-1} for the 315 and 515 nm lights in (c).

time (τ_{Rec}) after switching off the UV light was calculated to be 14.1 s using double exponential analysis. The good repeatability of the photovoltage response is also notable. Surprisingly, the periodic response of the PVA- and PSS-incorporated devices exhibited not only improved ΔV of 45 ± 2.0 and 63 ± 3.6 mV, respectively, but also shortened τ_{Rec} values of 11.6 and 3.12 s, respectively (Figure 4h,i and Table 1). Thus, the introduction of hydrophilic polymers improves the UV sensitivity and response/recovery speed, which is highly preferred for sensing applications. Furthermore, among representative self-powered photodetectors, our device exhibited a considerably faster response and restoration time for wavelength recognition (Table S1).

We further demonstrated its color-sensing performance (Figure 5). Upon irradiation with 375 and 530 nm lights at different intensities, the voltage change ($\Delta V/V_0$) showed a distinct trend depending on the light intensity ratio. At a high 375 nm intensity (I_{375}) and low 530 nm intensity (I_{530}) corresponding to the left top part in the figure, $\Delta V/V_0$ became significantly negative. In contrast, low I_{375} and high I_{530} irradiation, corresponding to the bottom right, resulted in a decreased change. Additionally, the total light intensity (or photon density) can be determined from the short-circuit current, as confirmed in our previous study [6]. Thus, our single-junction photodetector detects both the light intensity and color composition without a filter.

3 | Conclusion

We performed in situ XAS measurements under humidity-controlled conditions to reveal the water penetration behavior of PV devices. Adsorption of H_2O onto TiO_2 was observed in the O K-edge XAS spectra. By comparing the layered samples, the H_2O molecules were found to penetrate the devices and adsorb onto the mesoscopic TiO_2/ASIS composites. Accordingly, a photochemical reaction between the adsorbed water and charge carriers in TiO_2 was considered to have occurred. The possibly generated reactive species such as H^+ or/and OH^- were trapped at the ASIS/HTM and/or TiO_2/ASIS interfaces, serving as metastable charge traps. Based on these results, a hydrophilic polymer was incorporated into the device structure to enhance water permeation and retention. The response speed of the device with a PSS layer (τ_{UV} = 150 ms) was improved by one order of magnitude. Surprisingly, the PSS-incorporated device also exhibited an improved color sensitivity (ΔV) and recovery speed (τ_{Rec} = 3.12 s). These rapid responses are advantageous for sensing applications. Notably, our single-junction photodetector detected both the light intensity and color composition without a filter. Our work offers new insights into the mechanism of the WDPE and strategies for enhancing the wavelength responsiveness of single-junction multicolor sensing devices.

4 | Experimental Section

4.1 | SbSI:Sb$_2$S$_3$ (ASIS) Film Preparation

SbSI:Sb$_2$S$_3$ films were prepared according to our previous report [6, 40]. First, 0.22 M SbI_3 and 0.18 M $Sb(EtXa)_3$ were dissolved in dimethyl sulfoxide (DMSO). The solution was spin-coated at 2300 rpm for 30 s, followed by thermal annealing at 160°C for 5 min. The solution was spin-coated again, followed by thermal annealing at 240°C for 10 min. The thermal decomposition of metal-xanthate salts provides metal sulfides, which is known as Chugaev elimination [41].

4.2 | Photovoltaic Device Fabrication

An FTO substrate was cleaned with detergent, deionized water, and isopropyl alcohol. For TiO_2 deposition, a compact TiO_2 layer was deposited onto the FTO/glass via spray pyrolysis using a solution of titanium diisopropoxide bis(acetylacetonate) (Sigma Aldrich) in ethanol (1:12 v/v) at 450°C. A 200-nm-thick mesoporous-TiO_2 layer was deposited onto the compact TiO_2 layer by spin coating (5000 rpm, 30 s) diluted TiO_2 paste in ethanol (paste/ethanol = 1:7 w/w), followed by sintering at 500°C for 20 min. The substrates were then transferred to a N_2-filled glove box (O_2, H_2O < 0.1 ppm). An SbSI:Sb$_2$S$_3$ layer was deposited using the aforementioned procedure. HTM solution (10 mg mL^{-1} PCPDTBT in *o*-dichlorobenzene) was then

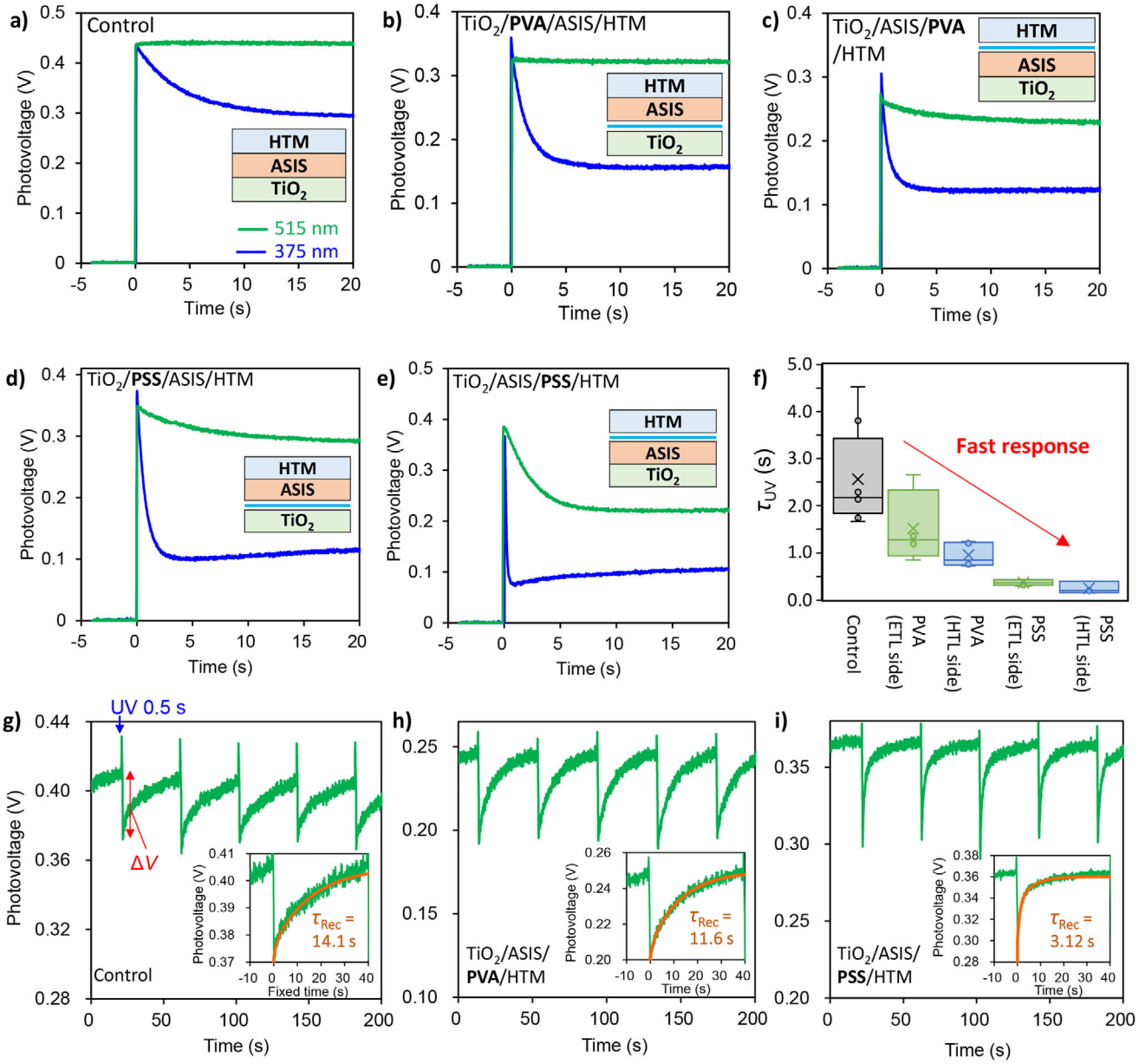

FIGURE 4 | TDPV decays of (a) the control device without interlayer, (b) with PVA at the TiO_2/ASIS interface, (c) with PVA at the ASIS/PCPDTBT interface, (d) with PSS at the TiO_2/ASIS interface, and (e) with PSS at the ASIS/PCPDTBT interface at 50% RH. The intensities of the 375 and 515 nm lights were modulated to yield same photocurrent values, as shown in Figure S11. (f) Response time (τ_{UV}) of the devices with different structures calculated by using double exponential fitting. Photovoltage response of (g) control, (h) PVA on ASIS, and (i) PSS on ASIS devices under periodic 375 nm UV irradiation (0.5 ± 0.1 s) with constant 515 nm irradiation. The UV irradiation was started after the photovoltage under 515 nm had stabilized. The insets show the fitting analysis of the recovery time after UV irradiation using double exponential equation.

spin-coated at 2000 rpm and annealed at 100°C for 10 min. Finally, a 70 nm thick Au electrode was deposited.

4.3 | Hydrophilic Polymer Interlayer Incorporation

For the devices with PVA or PSS, a thin polymer interlayer was introduced at the TiO_2/ASIS and/or ASIS/HTM interface by spin coating (2000 rpm, 30 s) the corresponding polymer solution (PVA: 5 mg mL^{-1} dissolved in DMSO, PSS: 0.5 vol% diluted with H_2O) onto the underlying layer, followed by drying, before depositing the subsequent layer. A PSS solution was prepared by diluting an 18 wt% PSS aqueous solution.

4.4 | Measurements

Photoabsorption spectroscopy (PAS) was performed using a JASCO V-730 spectrometer. Current–voltage curves were measured using a source meter unit (ADCMT Corp., 6241A) under a 100 mW cm^{-2} Xe lamp (Asahi Spectra MAX-303). The EQE spectra were measured using a Bunko Keiki SM-250KD instrument equipped with a Keithley 2401 source meter. The monochromated

TABLE 1 | Summary of photovoltage and photocurrent response characteristics of TiO_2/ASIS/HTM (control), TiO_2/ASIS/PVA/HTM, and TiO_2/ASIS/PSS/HTM devices.

	Control	PVA-incorporated	PSS-incorporated
R_{515} (mA W^{-1}) [a]	125.0 ± 28.1	42.7 ± 0.4	79.5 ± 17.2
τ_{UV} (s) [b]	2.56 ± 1.03	0.95 ± 0.25	0.25 ± 0.13
ΔV (mV) [c]	35 ± 2.2	45 ± 2.0	63 ± 3.6
τ_{Rec} (s) [d]	14.1	11.6	3.12

[a]Responsivity ($R = I/P$, where I and P represent the photocurrent and light power, respectively) under 515 nm light irradiation.
[b]UV response time (Figure 4f).
[c]UV-induced photovoltage change, and
[d]Recovery time from Figure 4g–i.

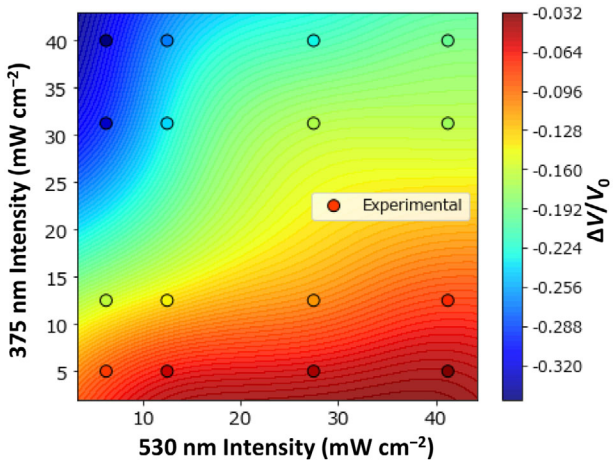

FIGURE 5 | Dependence of voltage change ratio ($\Delta V/V_0$) of a PSS-incorporated device upon the simultaneous irradiation of lights of different colors and intensities. ΔV and V_0 are the voltage change upon short 375 nm irradiation (0.5 ± 0.1 s) and base photovoltage under constant 530 nm irradiation, respectively, measured using the procedure described in Figure 4g–i. The background color is a fitting by radial basis function (RBF) interpolation. The data of a control device are also shown in Figure S13.

light power was calibrated using a silicon photovoltaic (PV) cell (Bunko Keiki model S1337-1010BQ).

4.5 | In Situ XAS Measurements

Soft X-ray absorption measurements were performed under humid conditions at the BL-2B beamline of the Photon Factory, KEK (Tsukuba, Japan). The partial fluorescence yield (PFY) mode using a silicon drift detector (SDD) was employed for the O K-edge, Ti L_3-edge, and Sb M-edge XAS measurements by integrating the fluorescence lines originating from each edge. The energy resolution of the SDD detector (Amptek, FAST SDD) was limited to approximately 100 eV. The film sample with the size of 5 mm × 5 mm was loaded onto a dedicated gas-flow measurement cell (see Figure S2). A 150 nm thick SiC membrane was placed on the film sample. The measurement cell was fixed onto the measurement window. A humidity sensor, gas inlet, and gas outlet were connected to the cell to precisely control the humidity [42–44]. Humid feed gas was allowed to flow through a small space between the film sample and the SiC membrane. After the humidity reached the target value, it was maintained for more than 10 min to promote H_2O adsorption and desorption before starting the measurement. The O K-edge XAS spectra were normalized only for the incident X-ray intensity (I_0) and baseline removal. The energy axes of the XAS spectra were corrected using the peak from the TiO_2 reference [36].

4.6 | TDPV and TDPC Measurements

A PV device was fabricated for TDPV and TDPC. The cathode and anode of the device were connected to an oscilloscope and a source meter, respectively. The output voltage of the source meter was set to ground (0 V). The intensities and the spot sizes of the 375 and 515 nm continuous wave lasers were modulated using neutral density (ND) filters and a concave lens ($f = 50$ mm), respectively. A 2 mm × 2 mm mask was placed in front of the device. The termination of the oscilloscope was 1 MΩ for the TDPV measurements and 50 Ω for the TDPC measurements. The control and sample data were obtained at approximately the same humidity (50% RH) with using a chamber to exclude the effect of vapor.

4.7 | Statistics

The average and standard deviation (SD) of the photodetection performances were calculated, and the values were described as mean ± SD in the corresponding figure caption or table. The number of data points for each statistic is also indicated.

Acknowledgements

This work was supported by the Japan Society for the Promotion of Science (JSPS) with the KAKENHI Grant-in-Aid for Scientific Research (A) (JP24H00484), KAKENHI Grant-in-Aid for Early-Career Scientists (JP23K13826), KAKENHI Grant-in-Aid for Scientific Research (B) (JP25K01857), KAKENHI Grant-in-aid for Scientific Research (A): Dynamic Exciton (JP20H05836), KAKENHI Grand-in-Aid for Scientific Research on Innovative Area: Aquatic Functional Materials (JP19H05717 and JP22H04541), KAKENHI Grant-in-Aid for Transformative Research Areas (A) "Supra-ceramics" (JP22H05145 and JP23H04626), Japan Science and Technology Agency (JST) CREST (JPMJCR23O2), JST SPRING (JPMJSP2138), a research grant from The Mazda Foundation, Yashima

Environment Technology Foundation. Soft X-ray absorption measurements were performed at the Photon Factory BL-2B with the approval of the Photon Factory Program Advisory Committee (Proposal No. 2023G662).

Conflicts of Interest

The authors declare no conflicts of interest.

Data Availability Statement

The data that support the findings of this study are available from the corresponding author upon reasonable request.

References

1. P. Wang, S. S. Liu, W. J. Luo, et al., "Arrayed Van Der Waals Broadband Detectors for Dual-Band Detection," *Advanced Materials* 29 (2017): 1604439, https://doi.org/10.1002/adma.201604439.

2. S. Lefler, R. Vizel, E. Yeor, et al., "Multicolor Spectral-Specific Silicon Nanodetectors Based on Molecularly Embedded Nanowires," *Nano Letters* 18 (2018): 190–201, https://doi.org/10.1021/acs.nanolett.7b03873.

3. E. A. Plis, N. Gautam, M. N. Kutty, et al., "Performance of Long-Wave Infrared InAs/GaSb Strained Layer Superlattice Detectors for the Space Applications," *Proceedings of the SPIE* 8164 (2011): 81640S.

4. W. Shockley, "The Theory of p-n Junctions in Semiconductors and p-n Junction Transistors," *Bell System Technical Journal* 28 (1949): 435–489, https://doi.org/10.1002/j.1538-7305.1949.tb03645.x.

5. F. S. Goucher, G. L. Pearson, M. Sparks, G. K. Teal, and W. Shockley, "Theory and Experiment for a Germanium p–n Junction," *Physical Review* 81 (1951): 637–638, https://doi.org/10.1103/PhysRev.81.637.2.

6. R. Nishikubo, S. Li, and A. Saeki, "Unprecedented Wavelength Dependence of an Antimony Chalcohalide Photovoltaic Device," *Advanced Functional Materials* 32 (2022): 2201577, https://doi.org/10.1002/adfm.202201577.

7. T. Kobayashi, R. Nishikubo, Y. Chen, K. Marumoto, and A. Saeki, "Wavelength-Recognizable SbSI:Sb_2S_3 Photovoltaic Devices: Elucidation of the Mechanism and Modulation of Their Characteristics," *Advanced Functional Materials* 32 (2023): 2311794.

8. R. Nie, H. S. Yun, M. J. Paik, et al., "Efficient Solar Cells Based on Light-Harvesting Antimony Sulfoiodide," *Advanced Energy Materials* 8 (2018): 1701901, https://doi.org/10.1002/aenm.201701901.

9. R. Nie, J. Im, and S. I. Seok, "Efficient Solar Cells Employing Light-Harvesting $Sb_{0.67}Bi_{0.33}SI$," *Advanced Materials* 31 (2019): 1808344, https://doi.org/10.1002/adma.201808344.

10. Y. C. Choi, E. Hwang, and D. H. Kim, "Controlled Growth of SbSI Thin Films from Amorphous Sb_2S_3 for Low-Temperature Solution Processed Chalcohalide Solar Cells," *APL Materials* 6 (2018): 121108, https://doi.org/10.1063/1.5058166.

11. K. Mistewicz, W. Matysiak, M. Jesionek, et al., "A Simple Route for Manufacture of Photovoltaic Devices Based on Chalcohalide Nanowires," *Applied Surface Science* 517 (2020): 146138, https://doi.org/10.1016/j.apsusc.2020.146138.

12. S. Inagaki, M. Nakamura, H. Hatada, et al., "Growth of Visible-Light-Responsive Ferroelectric SbSI Thin Films by Molecular Beam Epitaxy," *Applied Physics Letters* 116 (2020): 072902, https://doi.org/10.1063/1.5142642.

13. K. T. Butler, J. M. Frost, and A. Walsh, "Ferroelectric Materials for Solar Energy Conversion: Photoferroics Revisited," *Energy & Environmental Science* 8 (2015): 838–848, https://doi.org/10.1039/C4EE03523B.

14. K. Mistewicz, M. Nowak, R. Paszkiewicz, and A. Guiseppi-Elie, "SbSI Nanosensors: From Gel to Single Nanowire Devices," *Nanoscale Research Letters* 12 (2017): 334, https://doi.org/10.1186/s11671-017-1854-x.

15. M. Tamilselvan and A. J. Bhattacharyya, "Antimony Sulphoiodide (SbSI), a Narrow Band-Gap Non-Oxide Ternary Semiconductor with Efficient Photocatalytic Activity," *RSC Advances* 6 (2016): 105980–105987.

16. C. Wang, M. Zhang, Y. Fang, et al., "SbSI Nanocrystals: An Excellent Visible Light Photocatalyst with Efficient Generation of Singlet Oxygen," *ACS Sustainable Chemistry & Engineering* 6 (2018): 12166–12175, https://doi.org/10.1021/acssuschemeng.8b02498.

17. S. Dhar, P. Chakraborty, T. Majumder, and S. P. Mondal, "CdS-Decorated Al-Doped ZnO Nanorod/Polymer Schottky Junction UV–Vis Dual-Wavelength Photodetectors," *ACS Applied Nano Materials* 1 (2018): 3339–3345.

18. Y. Zhang, W. Xu, X. Xu, J. Cai, W. Yang, and X. Fang, "Self-Powered Dual-Color UV–Green Photodetectors Based on SnO_2 Millimeter Wire and Microwires/$CsPbBr_3$ Particle Heterojunctions," *The Journal of Physical Chemistry Letters* 10 (2019): 836–841, https://doi.org/10.1021/acs.jpclett.9b00154.

19. M. Dai, H. Chen, R. Feng, et al., "A Dual-Band Multilayer InSe Self-Powered Photodetector with High Performance Induced by Surface Plasmon Resonance and Asymmetric Schottky Junction," *ACS Nano* 12 (2018): 8739–8747, https://doi.org/10.1021/acsnano.8b04931.

20. L. Li, H. Chen, Z. Fang, et al., "An Electrically Modulated Single-Color/Dual-Color Imaging Photodetector," *Advanced Materials* 32 (2020): 1907257, https://doi.org/10.1002/adma.201907257.

21. Z. Lan and F. Zhu, "Electrically Switchable Color-Selective Organic Photodetectors for Full-Color Imaging," *ACS Nano* 15 (2021): 13674–13682.

22. Y. Chang, L. Huang, Y. Zhou, J. Wang, and W. Zhai, "Controlled Localized Phase Transition of Selenium for Color-Selective Photodetectors," *ACS Applied Materials & Interfaces* 14 (2022): 5624–5633, https://doi.org/10.1021/acsami.1c22909.

23. P. Szaniawski, J. Lindahl, T. Törndahl, U. Zimmermann, and M. Edoff, "Light-Enhanced Reverse Breakdown in Cu(In,Ga)Se_2 Solar Cells," *Thin Solid Films* 535 (2013): 326–330, https://doi.org/10.1016/j.tsf.2012.09.022.

24. L. Min, Y. Zhou, H. Sun, et al., "Carrier Dynamic Identification Enables Wavelength and Intensity Sensitivity in Perovskite Photodetectors," *Light: Science & Applications* 13 (2024): 280, https://doi.org/10.1038/s41377-024-01636-6.

25. A. Maurano, C. G. Shuttle, R. Hamilton, et al., "Transient Optoelectronic Analysis of Charge Carrier Losses in a Selenophene/Fullerene Blend Solar Cell," *The Journal of Physical Chemistry C* 115 (2011): 5947–5957, https://doi.org/10.1021/jp109697w.

26. G. Juska, K. Arlauskas, M. Viliu, K. Genevicius, R. Österbacka, and H. Stubb, "Charge Extraction by Linearly Increasing Voltage: A New Method for Determining Carrier Mobility in Thin Films,"*American Physical Society* 62 (2000): 235–238.

27. A. J. Mozer, G. Dennler, and A. Pivrikas, "Time-Dependent Mobility and Recombination of the Photoinduced Charge Carriers in Conjugated Polymer/Fullerene Bulk Heterojunction Solar Cells," *Physical Review B* 72 (2005): 035217, https://doi.org/10.1103/PhysRevB.72.035217.

28. T. Nagamori and K. Marumoto, "Direct Observation of Hole Accumulation in Polymer Solar Cells during Device Operation Using Light-Induced Electron Spin Resonance," *Advanced Materials* 25 (2013): 2362–2367, https://doi.org/10.1002/adma.201204015.

29. M. Namatame, M. Yabusaki, T. Watanabe, Y. Ogomi, S. Hayase, and K. Marumoto, "Direct Observation of Dramatically Enhanced Hole Formation in a Perovskite-Solar-Cell Material Spiro-OMeTAD by Li-TFSI Doping," *Applied Physics Letters* 110 (2017): 123904, https://doi.org/10.1063/1.4977789.

30. M. Suzuki, S. Murayama, N. Umesaki, and T. Tanaka, "Hydroxyl-Group Identification Using O K-Edge XAFS in Porous Glass Fabricated by Hydrothermal Reaction and Low-Temperature Foaming," *Molecules* 24 (2019): 3488, https://doi.org/10.3390/molecules24193488.

31. S. Benkoula, O. Sublemontier, M. Patanen, et al., "Water Adsorption on TiO_2 Surfaces Probed by Soft X-ray Spectroscopies: Bulk Materials vs.

isolated Nanoparticles," *Scientific Reports* 5 (2015): 15088, https://doi.org/10.1038/srep15088.

32. A. R. Abid, M. Mailhiot, N. Boudjemia, et al., "The Effect of Relative Humidity on $CaCl_2$ Nanoparticles Studied by Soft X-ray Absorption Spectroscopy," *RSC Advances* 11 (2021): 2103–2111.

33. Y. B. Kwon, B. M. Weon, K. H. Won, J. H. Je, Y. Hwu, and G. Margaritondo, "X-ray-Induced Changes in Wettability," *Langmuir* 25 (2009): 1927–1929, https://doi.org/10.1021/la804081k.

34. A. Nilsson, D. Nordlund, I. Waluyo, et al., "X-ray Absorption Spectroscopy and X-ray Raman Scattering of Water and Ice; An Experimental View," *Journal of Electron Spectroscopy and Related Phenomena* 177 (2010): 99–129, https://doi.org/10.1016/j.elspec.2010.02.005.

35. D. Nordlund, H. Ogasawara, K. J. Andersson, et al., "Sensitivity of X-ray Absorption Spectroscopy to Hydrogen Bond Topology," *Physical Review B* 80 (2009): 233404, https://doi.org/10.1103/PhysRevB.80.233404.

36. M. A. Van Spronsen, X. Zhao, M. Jaugstetter, et al., "Interface Sensitivity in Electron/Ion Yield X-ray Absorption Spectroscopy: The TiO_2–H_2O Interface," *Journal of Physical Chemistry Letters* 12 (2021): 10212–10217.

37. F. Fasulo, G. Piccini, A. B. Muñoz-García, M. Pavone, and M. Parrinello, "Dynamics of Water Dissociative Adsorption on TiO_2 Anatase (101) at Monolayer Coverage and below," *The Journal of Physical Chemistry C* 126 (2022): 15752–15758, https://doi.org/10.1021/acs.jpcc.2c03077.

38. K. R. Hahn, A. Tricoli, G. Santarossa, A. Vargas, and A. Baiker, "First Principles Analysis of H_2O Adsorption on the (110) Surfaces of SnO_2, TiO_2 and Their Solid Solutions," *Langmuir* 28 (2012): 1646–1656, https://doi.org/10.1021/la204124p.

39. T. Petit, J. Ren, S. Choudhury, et al., "X-Ray Absorption Spectroscopy of TiO_2 Nanoparticles in Water Using a Holey Membrane-Based Flow Cell," *Advanced Materials Interfaces* 4 (2017): 1700755, https://doi.org/10.1002/admi.201700755.

40. R. Nishikubo, H. Kanda, I. Garcia-Benito, et al., "Optoelectronic and Energy Level Exploration of Bismuth and Antimony-Based Materials for Lead-Free Solar Cells," *Chemistry of Materials* 32 (2020): 6416–6424, https://doi.org/10.1021/acs.chemmater.0c01503.

41. Y. T. Alharbi, F. Alam, A. Salhi, M. Missous, and D. J. Lewis, "Direct Synthesis of Nanostructured Silver Antimony Sulfide Powders from Metal Xanthate Precursors," *Scientific Reports* 11 (2021): 3053, https://doi.org/10.1038/s41598-021-82446-3.

42. K. Yamazoe, Y. Higaki, Y. Inutsuka, et al., "Enhancement of the Hydrogen-Bonding Network of Water Confined in a Polyelectrolyte Brush," *Langmuir* 33 (2017): 3954–3959, https://doi.org/10.1021/acs.langmuir.7b00243.

43. R. Watanabe, T. Sakamoto, K. Yamazoe, J. Miyawaki, T. Kato, and Y. Harada, "Ion Selectivity of Water Molecules in Subnanoporous Liquid-Crystalline Water-Treatment Membranes: A Structural Study of Hydrogen Bonding," *Angewandte Chemie International Edition* 59 (2020): 23461–23465.

44. K. Yamazoe, Y. Higaki, Y. Inutsuka, J. Miyawaki, A. Takahara, and Y. Harada, "Critical In-Plane Density of Polyelectrolyte Brush for the Ordered Hydrogen-Bonded Structure of Incorporated Water," *Langmuir* 38 (2022): 3076–3081, https://doi.org/10.1021/acs.langmuir.1c02895.

Supporting Information

Additional supporting information can be found online in the Supporting Information section.

Supporting File: adfm76809-sup-0001-SuppMat.pdf.